

Cite as: Appl. Phys. Rev. 8, 031408 (2021); doi: 10.1063/5.0053884

Submitted: 12 April 2021 · Accepted: 13 July 2021 ·

Published Online: 30 July 2021







Zhengjie Huang,¹ Shai R. Vardeny,² Tonghui Wang,³ Zeeshan Ahmad,⁴ (D) Ashish Chanana,⁵ (D) Eric Vetter,^{1,3} Shijia Yang,¹ Xiaojie Liu,⁵ Giulia Galli,^{4,6,7} (D) Aram Amassian,^{3,a)} (D) Z. Valy Vardeny,^{5,a)} (D) and Dali Sun^{1,a)} (D)

AFFILIATIONS

- ¹Department of Physics and Organic and Carbon Electronics Lab (ORaCEL), North Carolina State University, Raleigh, North Carolina 27695, USA
- ²Center for Integrated Nanotechnologies, Los Alamos National Laboratory, Los Alamos, New Mexico, 87545, USA
- ³Department of Materials Science and Engineering and Organic and Carbon Electronics Lab (ORaCEL), North Carolina State University, Raleigh, North Carolina 27695, USA
- ⁴Pritzker School of Molecular Engineering, University of Chicago, Chicago, Illinois 60637, USA
- ⁵Department of Physics and Astronomy, University of Utah, Salt Lake City, Utah 84112, USA
- ⁶Department of Chemistry, University of Chicago, Chicago, Illinois 60637, USA
- ⁷Argonne National Laboratory, Lemont, Illinois 60439, USA

ABSTRACT

Hybrid organic-inorganic perovskites (HOIPs) are prime candidates for studying Rashba effects due to the heavy metal and halogen atoms in their crystal structure coupled with predicted inversion symmetry breaking. Nevertheless, observation of the Rashba effect in cubic CH₃NH₃PbBr₃ single crystals that possess bulk inversion symmetry is the subject of extensive debate due to the lack of conclusive experiments and theoretical explanations. Here, we provide experimental evidence that *Rashba state* in cubic CH₃NH₃PbBr₃ single crystals at room temperature occurs exclusively on the crystal surface and depends on specific surface termination that results in local symmetry breaking. We demonstrate this using a suite of spatially resolved and depth-sensitive techniques, including circular photogalvanic effect, inverse spin Hall effect, and multiphoton microscopy, that are supported by first principle calculations. Our work suggests using surface Rashba states in these materials for spintronic applications.

Published under an exclusive license by AIP Publishing. https://doi.org/10.1063/5.0053884

INTRODUCTION

The Rashba spin-splitting state is an archetypal quantum phenomenon in which the spin and momentum are locked. $^{1-4}$ It causes splitting of a doubly spin-degenerate continuum electronic band into two subbands shifted with respect to each other in k space by $2k_0$ (Fig. 1) and is commonly represented by two displaced circular Fermi contours. At k_0 , a minimum arises at depth E_0 . This splitting is described by the Rashba coefficient (α_R), as defined by $\alpha_R = 2E_0/k_0$. The Rashba effect can split differently the valence and conduction band edges, resulting in an indirect bandgap semiconductor. Two preconditions need to be satisfied for the occurrence of Rashba splitting: (i) the presence of heavy elements (such as lead) that introduce strong spin-orbit coupling (SOC) and (ii) the lack of inversion symmetry, which is satisfied in the bulk of non-centrosymmetric crystals or at the crystal's surfaces, interfaces, and grain boundaries. The Rashba effect

has revolutionized the field of spintronics, making it possible to envision the next generation of pure spin current generators, transmitters, and detectors. ^{5–9} This enhanced interest has led to a broad exploration of novel Rashba materials.

Hybrid organic-inorganic metal halides have attracted immense attention in recent years, mostly due to the remarkable success of lead halide perovskites in photovoltaic and light-emitting diode applications. These materials can be classified as 3D perovskites adopting AMX₃ composition or as layered perovskites also known as quasi-2D perovskites adopting Ruddlesden–Popper and Dion–Jacobson compositions. Broadly referred to as hybrid organic-inorganic perovskites (HOIPs), these soft ionic semiconductors are amenable to solution-phase processing as well as conducive to facile growth of macroscopic single crystals (SCs) while maintaining excellent optoelectronic properties. The HOIPs have also shown a diversity of interesting properties,

^{a)}Authors to whom correspondence should be addressed: aamassi@ncsu.edu; val@physics.utah.edu; and dsun4@ncsu.edu

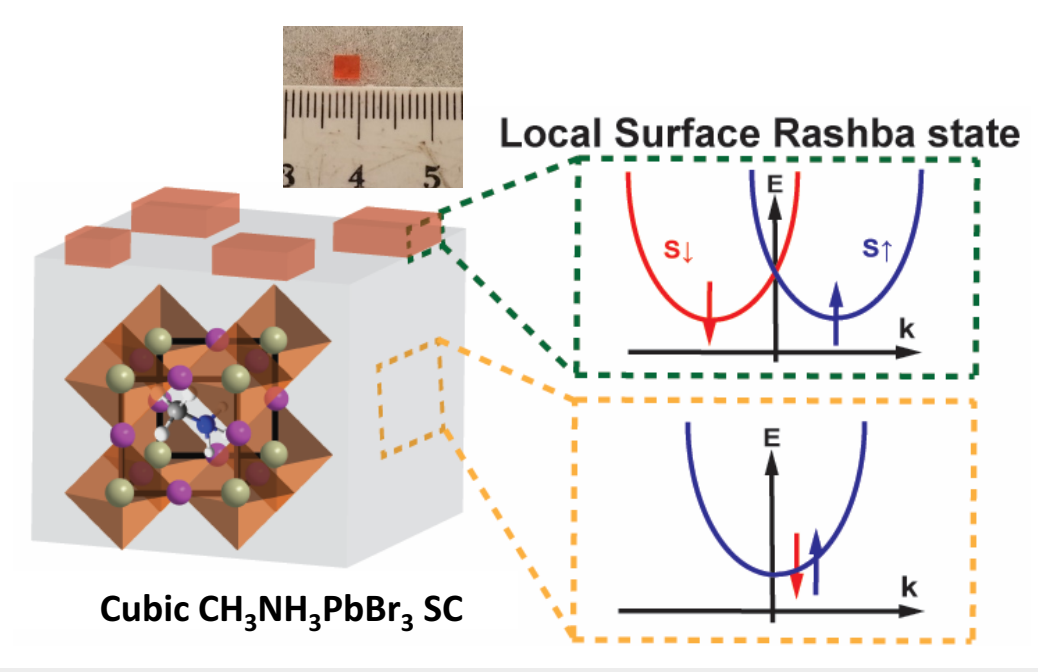


FIG. 1. Schematic illustration of Rashba state domains on the surface of a cubic MAPbBr₃ SC due to the presence of local symmetry breaking. The spin split in the conduction band is shown for the domains on the crystal surface due to the Rashba effect (top panel) but not in the bulk (bottom panel).

including long carrier lifetimes of up to tens of microseconds, ¹⁴ quantum confinement, ^{15–17} ferroelectricity, ^{18,19} and enhanced inherent stability. ²⁰ The long carrier lifetimes are particularly surprising given that most HOIP films are polycrystalline and tend to be highly defective. However, because HOIPs involve heavy metals that possess an intrinsically large SOC, a leading hypothesis to explain the slow carrier recombination has been the formation of a large, static/dynamic bulk Rashba effect that results in an indirect bandgap. ^{21,22} This assumption has led to a myriad of density functional theory (DFT) calculations that have examined the Rashba effect in various HOIP structures. ^{23,24} However, the Rashba effect in 3D HOIPs has been the subject of extensive debate, given conflicting experimental evidence. ^{32–34} The reason for that is the lack of ample experimental tools for directly measuring the Rashba effect.

For example, a giant Rashba effect was first reported in CH₃NH₃PbBr₃ (MAPbBr₃) SCs using angle-resolved photoemission spectroscopy (ARPES).²⁸ It was found that the Rashba parameter, α_R is 7 ± 1 and $11 \pm 4 \,\text{eV} \cdot \text{Å}$ in the orthorhombic (at low temperature) and the cubic (at room temperature) phases, respectively. A recent systematic study of the circular photogalvanic effect (CPGE),^{29,3} observation of helicity-dependent photocurrent, indicated a dynamical Rashba effect in the tetragonal phase of MAPbI₃ SCs.³⁰ Indirect tail states arising from the dynamic Rashba effect in MAPbBr₃ SCs has been observed where the dynamic inversion symmetry is broken by thermally induced structural polar fluctuations at elevated temperatures.³¹ However, it has also been reported that the predicted static bulk Rashba effect in 3D HOIPs may be an artifact of DFT calculations.³² Furthermore, the needed inversion symmetry breaking has not been observed in the bulk of MAPbBr3 samples using second harmonic generation spectroscopy. 32 More recently, no clear Rashba splitting has been observed in MAPbBr₃ SCs in the valence band using the

ARPES method. 33,34 It is noteworthy that MAPbBr $_3$ forms a somewhat disordered cubic structure at room temperature, having an "average" space group symmetry of $Pm\overline{3}m$ due to the free rotation attributed to the MA $^+$ cations induced by thermal fluctuation. This "pseudocentrosymmetric" structure possesses inversion symmetry and, thus, should not support a bulk Rashba effect unless an intrinsic surface reconstruction occurs at low temperatures. The Recall that ARPES is a surface-sensitive technique, whereas CPGE is regarded as a bulk method. In any case, these inconsistencies and conflicts call for further investigation of the Rashba effect in MAPbBr $_3$ SCs using a multipronged strategy.

We examine in this work the existence of the Rashba state in MAPbBr₃ SCs at room temperature that apparently does not possess a static inversion symmetry breaking.³² Using the CPGE technique, we observed a substantial helicity-dependent photocurrent response when excited with circularly polarized light. Also by utilizing the excellent optoelectronic properties of MAPbBr3, we successfully demonstrate the photoinduced inverse spin Hall effect (photo-ISHE) in a MAPbBr₃ SC/Pt heterostructure.^{36,37} This experiment unravels the spin texture related to the helicity-dependent photocurrent that is measured by the CPGE technique. It also provides unambiguous proof for the existence of surface Rashba states on MAPbBr₃ surfaces but not in bulk (Fig. 1). In addition, the magnetic field orientation dependence of the Hanle effect^{38,39} related to the photo-ISHE response further validates the spin texture on the crystal surface. We also used multiphoton microscopy (MPM)^{40–43} in combination with spatially resolved photo-ISHE measurements to show the existence of domains on the crystal's surface that exhibit various degrees of Rashba effect, depending on the surface termination, in agreement with our DFT calculations. By reconstructing different surface terminations along the MAPbBr3 crystal, we found that the Rashba parameter varies between null and \sim 2.02 eV,

which can account for the observed inhomogeneity of the Rashba states. These results offer a cautionary note in measuring and reporting this important phenomenon in 3D HOIPs at room temperature.

CIRCULAR PHOTOGALVANIC EFFECT AND PHOTOINDUCED INVERSE SPIN HALL EFFECT

In the CPGE experiment, we resonantly generated photocurrent in MAPbBr3 SCs with circularly polarized light to clarify the existence of spin splitting in the band structure. 29,30 CPGE is an intriguing quantum phenomenon, namely, a photovoltaic effect that does not require a built-in electric field. This process directly converts the angular momentum of the photons to electron-spin polarization, enabling the integration of polarized light in spintronic technologies. For a typical Rashba-type band structure, the interband optical transition between the spin-polarized valence and conduction bands depends on the helicity of the incident light [Fig. 2(a)]. Since the associated group velocities dE/dk differ in sign in each spin-split band, the resulting transverse spin-aligned (i.e., S_x along $\pm x$ direction) photocurrent reverses its polarity (i.e., J_C along $\pm y$ direction) when the light helicity is switched. The dependence of $J_c(CPGE)$ on the rotation angle of the $\lambda/4$ waveplate (α) may be described by an oscillating function that consists of three terms:29

$$J_c(CPGE) = Csin(2\alpha) + Lcos(4\alpha) + D,$$
 (1)

where D is the polarization-independent photocurrent offset, and C and L are, respectively, the circular and linear photogalvanic effect coefficients (namely, CPGE and LPGE), which depend on the laser incidence angle θ .^{29,30} The C term describes the effect of light helicity on the photocurrent and quantifies the difference between photocurrent excited using left-circularly polarized (LCP) and right-circularly polarized (RCP) light.^{29,30} LPGE, the term with coefficient L, is usually induced by asymmetric electron scattering with phonons or optical beam anisotropy (e.g., optical ellipticity) that is helicity independent and does not change with illumination by left-handed to right-handed circular polarization. Figures 2(b) and 2(c) present the measured helicity dependence of the photocurrent (J_{CPGE}) at two different out-ofplane inclination angles: θ of $\pm 50^{\circ}$ as a function of the $\lambda/4$ waveplate rotation angle a. A laser with polarized light at 450 nm and power of P = 1 mW was used to excite the MAPbBr₃ SC sample that had two electrical contacts \sim 500 μ m apart. Note that the laser photon energy $\hbar\omega = 2.75\,\text{eV}$ is above the energy gap E_g of the MAPbBr3 $(E_g$ \sim 2.3 eV). In Fig. 2(c), the polarization-independent photocurrent background (i.e., the D term) has been subtracted from the data for clarity. This large photocurrent background is one order of magnitude higher than the C and L components, which can be attributed to the

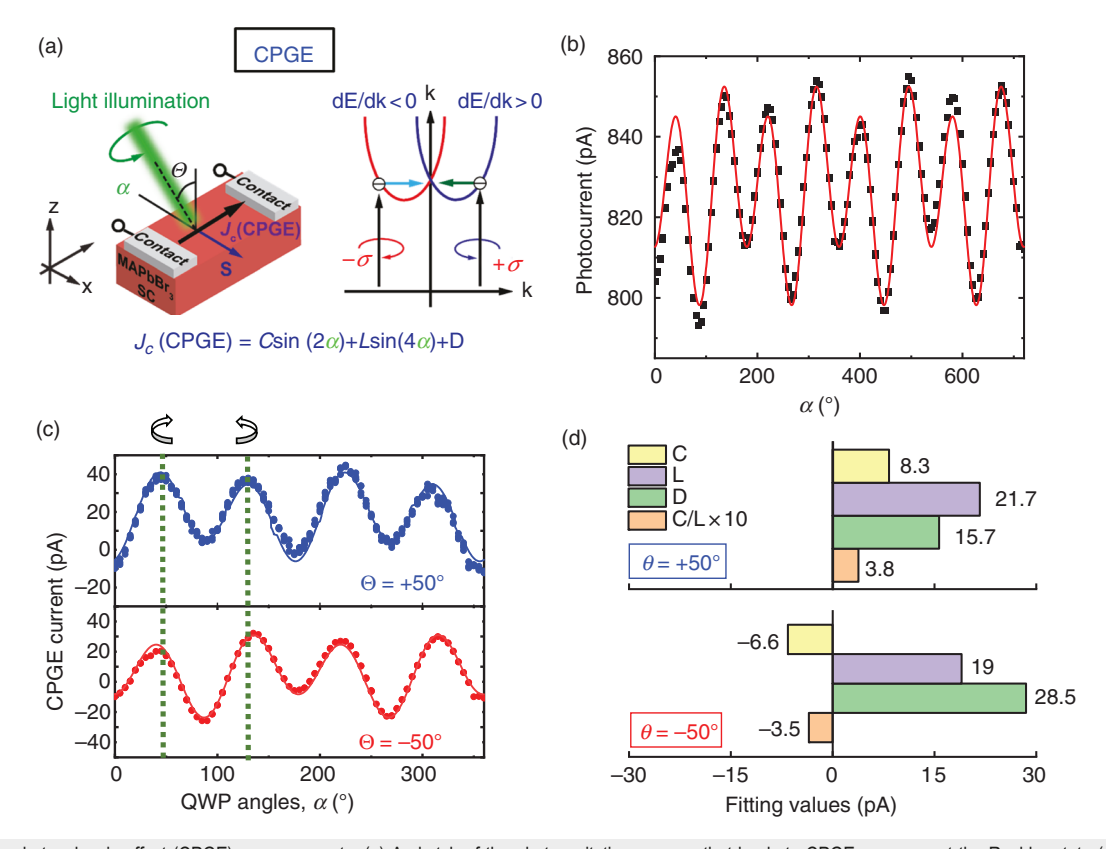


FIG. 2. Circular photogalvanic effect (CPGE) measurements. (a) A sketch of the photoexcitation process that leads to CPGE response at the Rashba state (right panel) and the CPGE experimental configuration where the angles α and θ are denoted (left panel). The bottom panel shows the equation that describes the resulting photocurrent at the Rashba state. (b) The obtained photocurrent response in the CPGE configuration as a function of the $\lambda/4$ waveplate rotation angle α . The line through the data points is a fit using Eq. (1). (c) Helicity-dependent photocurrent measured at two impinging angles: $\theta = +50^{\circ}$ (blue symbols), $\theta = -50^{\circ}$ (red symbols). The lines through the data points are fits using Eq. (1) with fitting parameters C, L, D, and C/L ratio, as shown in panel (d), having different colors. QWP, quarter-wave plate.

large photovoltaic effect in the MAPbBr₃ SC. It is clearly seen that the obtained photocurrent changes with α in a periodic fashion that can be well fitted using Eq. (1). Note that the fitted circular coefficient C changes sign when the incident light angle θ is reversed from $+50^{\circ}$ to -50° , with a maximum amplitude of 8.3 pA; in contrast, the linear photogalvanic coefficient L (\sim 19–22 pA) does not change sign with θ [Fig. 2(d)]. The C/L ratio at the two incident angles is 0.3, which is in agreement with the reported C/L ratio in MAPbI₃ SCs²⁹ and that in the layered perovskite $(PEA)_2PbI_4$.³⁰ Also, the coefficient $C(\theta)$ increases with θ approximately as $\sin(\theta)$ and vanishes at normal incidence $(\theta = 0)$, whereas the coefficient $L(\theta)$ exhibits a parabolic response (see Fig. S3). The dependence of both photocurrent components on α and θ proves the existence of the CPGE response in the MABr₃ SC, which, in turn, shows that this SC supports the existence of a Rashba state.2

To identify the spin texture characteristics in the photocurrent generated in the CPGE experiment, we conducted helicity-dependent photo-ISHE using a Pt overlayer as the spin detector^{36,37} [Fig. 3(a)]. The thin Pt overlayer (\sim 3 nm) is semitransparent at the laser wavelength, ensuring that the light excitation reaches the MAPbBr₃/Pt interface. Similar to the case of the CPGE measurement where the light illumination was directed onto the MAPbBr3 SC surface, here, under circular polarization illumination from the back, electrons with spin orientation polarized along the light propagation direction are photogenerated into the spin-polarized conduction band at the Rashba state due to the optical selection rules. Subsequently, the resulting photoinduced spin polarization diffuses as a pure spin current into the Pt overlayer across the MAPbBr₃ SC/Pt interface. In turn, the injected spin current is converted into an electromotive force $J_{photo-ISHE}$ along the $\pm y$ direction via the ISHE process in the adjacent Pt layer 44,45 having the strong spin-orbit interaction; this process may be described as follows:3

$$J_{photo-ISHE} = \theta_{ISHE} J_s(CPGE) \times S + J_c(CPGE),$$
 (2)

where the first term represents the ISHE process in the Pt layer, θ_{ISHE} is the spin Hall angle of the Pt layer, $I_s(CPGE)$ is the pure spin current that diffuses into the Pt overlayer from the MAPbBr₃ SC along the z direction, and S denotes the spin orientation. The second term in Eq. (2) arises from the photocurrent along the $\pm y$ direction that is directly generated by the CPGE process, which may partially penetrate into the Pt overlayer. However, this photocurrent is several orders of magnitude smaller than the ISHE current due to the efficient spin-tocharge conversion in the Pt overlayer. By detecting the photo-ISHE response, the degree of spin polarization from the helicity-dependent photocurrent of the CPGE in the MAPbBr₃ SC may be directly characterized. We anticipate that $J_{photo-ISHE}$ would hold similar light helicity dependence as that in the CPGE measurement.

The photo-ISHE measurement has been performed on the MAPbBr₃ SC/Pt bilayer to validate the spin-dependent character of the photocurrent under left- or right-circularly polarized illumination. Figures 3(b) and 3(c) show the photogenerated charge current across the Pt overlayer $(J_{photo-ISHE})$ at two light incidence angles θ . The obtained light helicity dependencies of the charge current in the Pt layer are consistent with the prediction of the photo-ISHE signal induced by photoexcited spin currents at the Rashba state.⁴⁶ While sharing a similar photocurrent response for the left- and rightcircularly polarized illumination in the CPGE configuration, the obtained C(photo-ISHE) coefficient for the Pt photocurrent (\sim 330 pA at $\theta = -50^{\circ}$) is about two orders of magnitude larger than that of C(CPGE) (~8 pA) in the same MAPbBr₃ sample. This can be attributed to the large spin-to-charge conversion efficiency in the Pt overlayer, as indicated by a much larger C/L ratio (up to 0.97) [see Fig. 3(d)]. The CPGE-generated spin-polarized photocurrent is estimated, using Eq. (2), as $J_S(CPGE) = 2 \times 10^6 \text{ A} \cdot \text{m}^{-2} \cdot \text{W}^{-1}$. Note that the obtained C(photo-ISHE) coefficient has an opposite sign compared to the C(CPGE) coefficient in the CPGE experiment described previously at the same incident angle. To explain this, we note that in the photo-ISHE experiment, the spin current diffuses along the +zdirection, which is opposite of that in the CPGE configuration. Having positive θ_{ISHE} , this may lead to an opposite sign of the generated charge current in the Pt layer, $J_{photo-ISHE} \propto J_s \times S$. Based on the previously measured short spin diffusion length in polycrystalline MAPbBr₃ thin films at room temperature (~ 3 nm),⁴⁷ the observed photo-ISHE signal indicates that the spin current in the Pt overlayer originates mainly from the CPGE current diffusion from the adjacent MAPbBr₃ interface⁴⁷ rather than from the bulk crystal, suggesting an interfacial Rashba state that occurs on the surface of MAPbBr₃ SC (as shown in the following sections).

HANLE EFFECT

Separation of the spin current from transverse photocurrent using the photo-ISHE technique enabled us to probe the spin lifetime of the Rashba state at the interface by measuring the Hanle effect;³ this method has been accepted as proof of spin-aligned current in organic semiconductors and HOIPs. 48-50 When an out-of-plane magnetic field, B_z , is applied perpendicular to the spin orientation (S_x) , it generates spin precession around the B_z direction, as illustrated in the top panel of Fig. 3(e). This leads to $J_{\text{photo-ISHE}}$ quenching that increases with the field B_z , which can be described by the following relation:⁵⁰

$$J_{photo-ISHE}(B_{z}) = \frac{J_{photo-ISHE}(B_{z}=0)}{1 + (\omega_{L}\tau_{tot})^{2}},$$

$$\frac{1}{\tau_{tot}} = \frac{1}{\tau_{s}(Pt)} + \frac{1}{\tau_{s}(Rashba)},$$
(3)

$$\frac{1}{\tau_{tot}} = \frac{1}{\tau (Pt)} + \frac{1}{\tau (Pashba)},\tag{4}$$

where $\omega_{\rm L} = \mu_{\rm B} g_{\rm ex} B_{\rm z}/\hbar$ is the Larmor frequency ($g_{\rm ex}$ is the g-factor of the electron spin). τ_{tot} is the spin lifetime at the MAPbBr₃/Pt interface, which is affected by both the surface Rashba state on the MAPbBr3 SC and the spin scattering inside the Pt overlayer. The spin lifetime τ_{tot} can thus be derived from the half width at half maximum of the obtained Hanle response. In contrast, when the magnetic field is applied in the direction of the spin orientation (e.g., B_x), no Hanle effect is possible.

Figure 3(e) presents the measured Hanle effect of the photo-ISHE response while applying an external magnetic field directed along +z, causing spin precession around the field B_z . This leads to quenching of the helicity-dependent C term in the photo-ISHE signal via the Hanle effect up to 8%. In contrast, the spin-independent background D shows only a subtle change with B that may be attributed to the magnetic field effect of the photocurrent in hybrid perovskite materials. In contrast, when the field is applied in the x direction, which is parallel to the spin polarization direction [Fig. 3(f)], no substantial Hanle effect is observed. The weak field dependence of the D component along with both field directions also excludes a possible

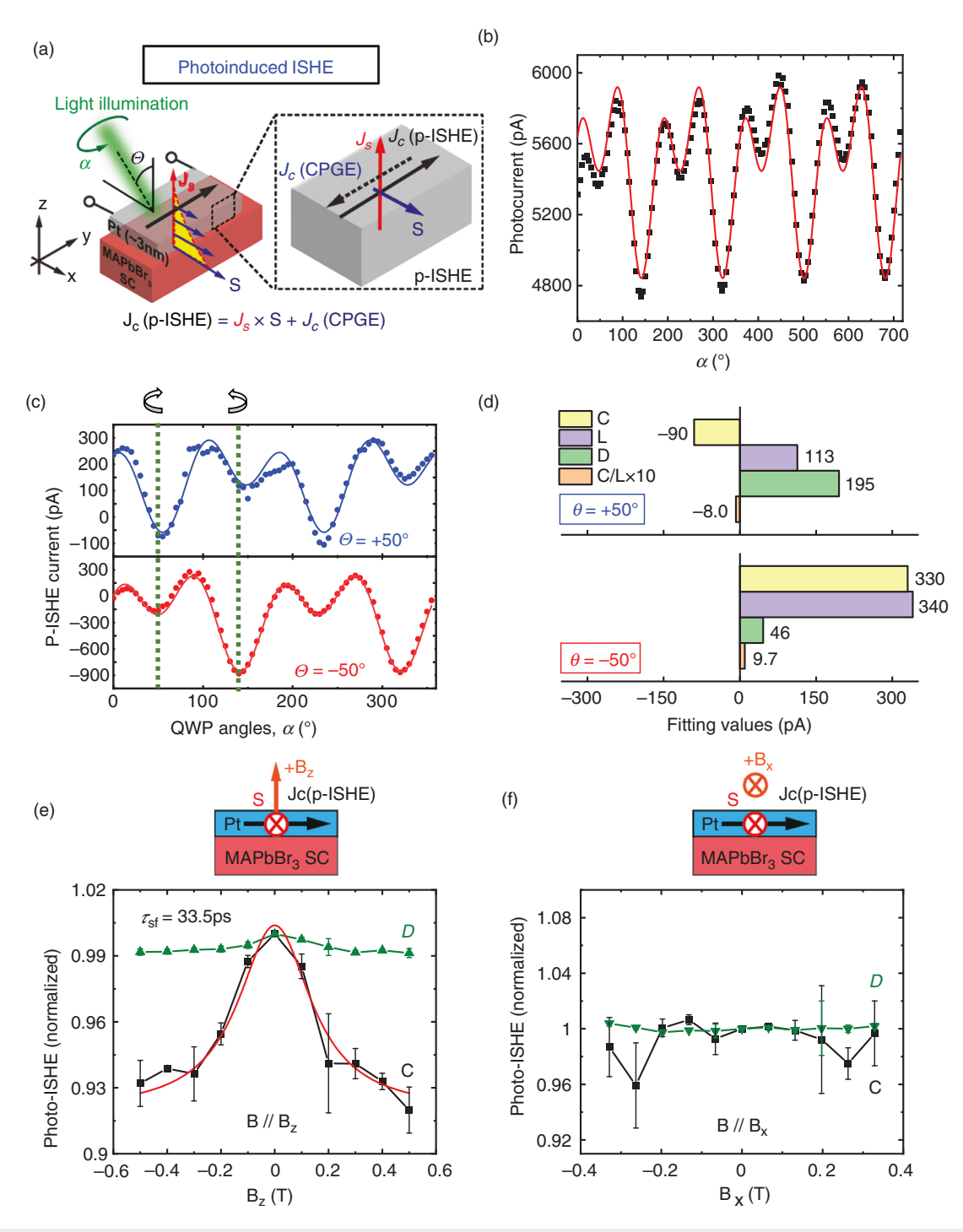


FIG. 3. Photoinduced ISHE measurements and the Hanle effect. (a) A sketch of the photo-ISHE configuration (left panel) at the MAPbBr₃ SC/Pt interface and the equation that describes its response. The right panel illustrates the spin diffusion from the MAPbBr₃ SC and the ISHE process in the Pt overlayer. (b) The photocurrent induced by the photo-ISHE as a function of the quarter-wave plate (QWP) rotation angle α . (c) Helicity-dependent photo-ISHE response vs α at two impinging light angles θ . The lines through the data points are fits using Eq. (1), where panel (d) depicts the fitting parameters C, L, D, and C/L ratio. (e) and (f) The Hanle effect showing field dependence of the photo-ISHE parameters when the field is applied out of plane [B_z, (e)] and in plane [B_x, (f)], respectively. The top insets depict the photo-ISHE sample configuration at the two field directions. The field-dependent C values in panel (e) are fitted using Eq. (3) (solid red lines) from which the spin relaxation time at the interface is estimated as $\tau_{tot} \sim 33.5 \, (\pm 1) \, \text{ps}$.

ordinary Hall effect, a planar Hall effect, and an anisotropy magnetoresistance that may overlap with the Hanle effect, validating the in-plane spin orientation (S_x) of the C component. The solid red line in Fig. 3(e) is a fit, using Eq. (3), from which we obtained $\tau_{tot}=33.5\pm1$ ps for both the L and C terms at T=300 K. Taking $\tau_s(Pt)=35.5\pm1$ ps from the oblique Hanle effect measured in a NiFe/Pt control sample, ⁴⁹ the spin lifetime at the Rashba state of MAPbBr₃ SC is estimated to be $\tau_s(Rashba)=\sim500\pm100$ ps. This value is in agreement with the obtained long spin lifetime measured by spin pumping in MAPbBr₃ SC. ⁴⁹

OBSERVATION OF SPATIALLY RESOLVED SURFACE RASHBA STATES

The observation of the Rashba effect by CPGE and photo-ISHE measurements in cubic MAPbBr3 SC phase that possesses inversion symmetry implies the existence of a substantial surface Rashba effect on the MAPbBr3 SC surface. To show this, we sought to directly observe the surface symmetry breaking, which is a precondition for Rashba splitting, using spatially resolved second-harmonic generation (SHG) measurements performed in the bulk and surface of the MAPbBr₃ SC samples by the MPM method^{40–43} (see Methods). Figure 4(a) shows the spatially resolved MPM image on the MAPbBr₃ SC surface⁴⁸ (see also Fig. S5) using a pulse laser at $1.55 \mu m$. The dominant green emission bands are due to third-harmonic generation (THG) at 517 nm and three-photon absorption-induced photoluminescence (TP-PL) at 550 nm; both occur regardless of inversion symmetry breaking.⁴³ No clear SHG signal is observed when the laser is focused inside the bulk of the crystal. In contrast, a weak SHG signal (i.e., the red emission between 750 and 800 nm) can be observed emanating only from the surface, consistent with our previous observations. 48 Whereas the existence of the SHG signal implies the presence of the symmetry breaking on the surface of the MAPbBr3, it is striking that its intensity is several orders of magnitude lower than that of the THG and TP-PL signals. Indeed, should the symmetry breaking be generalized to the whole surface of the MAPbBr₃ SC sample, a stronger SHG signal would undoubtedly be generated. We therefore conclude that the inversion symmetry breaking must be spatially localized in certain parts of the MAPbBr₃ SC surface. Closer investigation of spatially resolved MPM spectra shown in Figs. 4(b) and 4(c) confirms that the SHG signal indeed only appears at certain locations (delineated as red spots) on the SC surface. The surface of as-grown MAPbBr₃ SCs appears to reveal the presence of mounds and features, which are also observed by optical microscopy; these may be due to the termination process of the inverse temperature crystallization (ITC) crystal growth. First principle calculations described in the section DFT Calculations show that the Rashba coefficient and splitting for states on the surface depend on the surface terminations in support of the various domains on the MAPbBr₃ surface that possess different CPGE strength, ^{52–54} as measured experimentally.

Since the strength of the Rashba state determines the magnitude of the injected spin current into the Pt overlayer, we expect to observe a spatial distribution of the photo-ISHE signals across the MAPbBr₃ SC surface analogous to the MPM imaging. Figures 5(a) and 5(b) show the obtained 2D contour plots of the photocurrent background (i.e., the D term) and the helicity-dependent photo-ISHE component [i.e., the C(photo-ISHE) term]. The spatial distribution of the photocurrent background can be explained by the facet-dependent density of trap states,⁵⁵ which would not influence the strength of the Rashba states. Different from the spatial distribution of the helicityindependent photocurrent component, in the helicity-dependent photo-ISHE component, the C(photo-ISHE) varies significantly across the SC surface, ranging from 0 to 38 pA. To exclude the possible influence from the bulk photocurrent on the surface due to different reflections induced by the surface roughness and facet-dependent photovoltaic efficiency,⁵⁵ a normalized photo-ISHE component [i.e., *C/D* ratio, Fig. 5(c)] derived from the helicity-dependent measurement in each pixel is calculated. The *C/D* ratio varies from 0% to 4.9% across a large area of the SC surface (5 mm \times 5 mm). A similar distribution of the C/D ratio is also observed when the spatially resolved photo-ISHE measurement is measured in a smaller area (180 μ m \times 180 μ m) [Figs. 5(d) and 5(f)]. The observed C(photo-ISHE) term response changes from 67 pA to 144 pA, whereas the C/D ratio changes from 2.2% to 6%. This local distribution of the photo-ISHE signals further corroborates that the generated spin current excited by the LCP and RCP illuminations occurs in small domains on the surface (where the broken inversion symmetry is present), supporting the existence of domain-related surface Rashba states on MAPbBr3 SCs.

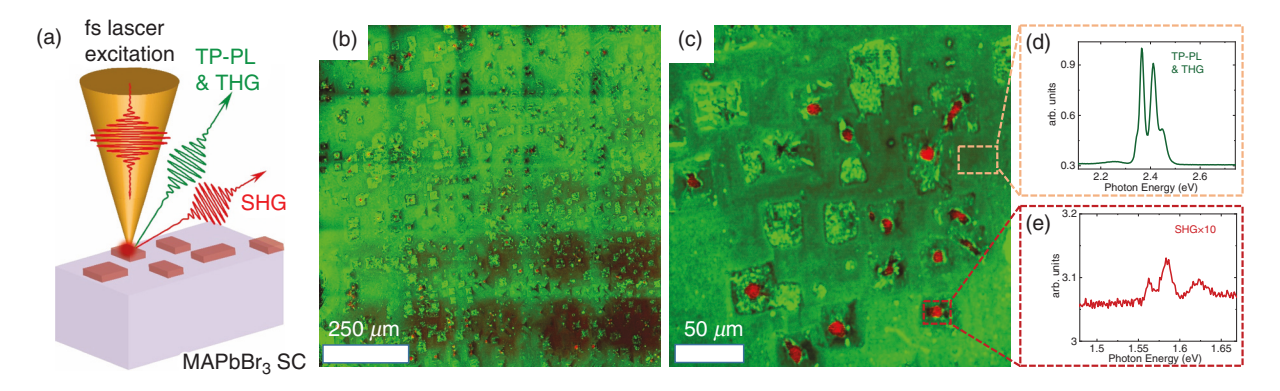


FIG. 4. Spatially resolved MPM measurements. (a) Schematic illustration of the MPM setup where the beam is focused on the MAPbB₃ SC surface with Rashba state domains. (b) and (c) The MPM response image in a large $(1.25 \times 1.25 \text{ mm}^2)$ and small $(250 \times 250 \text{ } \mu\text{m}^2)$ area of the SC sample. In both images, the green background originates from THG, whereas the red dots are from the SHG signal that occurs only at localized spots on the SC surface and are due to localized symmetry breaking. (d) and (e) The prototypical SHG, THG, and TP-PL emission spectra measured on the SC surface. arb., arbitrary.

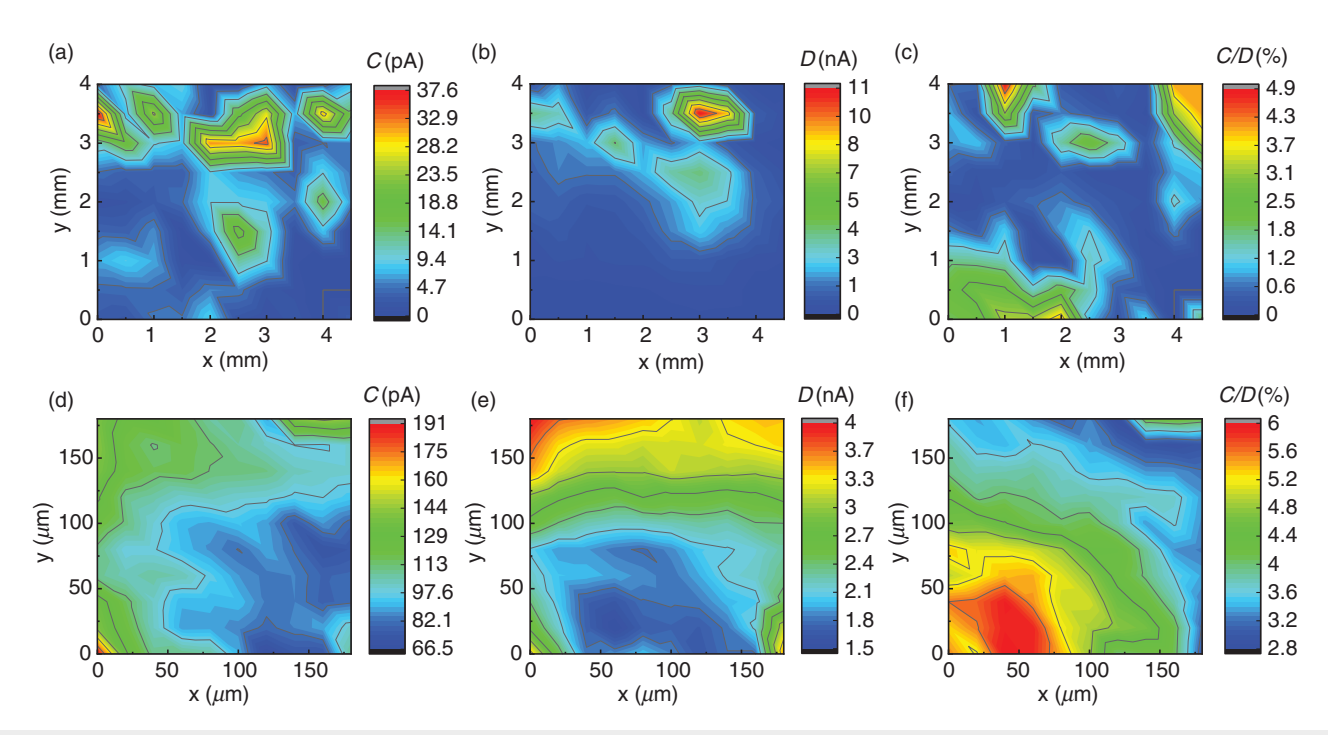


FIG. 5. Spatially resolved photo-ISHE measurements. (a)–(c) Spatially resolved helicity-dependent photo-ISHE component [C term in the PC(α) response], bulk photocurrent background (D term), and normalized C/D ratio on the surface of MAPbBr₃ SC/Pt sample (5 mm \times 5 mm), respectively. (d)–(f) Zoomed-in 2D contour plots of the obtained photo-ISHE parameters (C, D, and C/D ratio, respectively) obtained from a smaller area (180 μ m \times 180 μ m) of the MAPbBr₃ SC/Pt sample, respectively.

DFT CALCULATIONS

To understand the variability of the observed Rashba splitting, we performed DFT calculations for atomistic models of several possible terminations of the MAPbBr₃ (100) surface, as shown in Fig. 6(a). These configurations, named according to the species located at the surface (i.e., MABr, PbBr₂, PbBr, and Br), may be either thermodynamically stable or kinetically stabilized, depending on the synthesis conditions and the termination process of the ITC process. Based on experimental XPS spectra and STM imaging, it has been shown that an aged surface of a MAPbBr3 SC undergoes reconstruction due to adsorption of moisture. 56,57 Hence, we also considered hydrated PbBr₂- and MABr-rich surfaces in our study. As a representative calculation, we found the band structure of the MABr termination in Fig. 6(b), which shows that the valence band maximum (VBM) and the conduction band minimum (CBM) lie close to the M point (0.5,0.5) of the two-dimensional Brillouin zone. The band structures of other terminations are shown in Figs. S9-S15. In all cases considered here, after geometry optimization starting from positions with inversion symmetry, the atomistic configurations of the surfaces relax to a new geometry with lower symmetry. SOC breaks the degeneracy of the bands, resulting in the Rashba splitting seen in Fig. 6(b). The Rashba nature of the splitting is evident from the spin texture of the valence bands at the M point, one of which is shown in Fig. 6(c).

To quantify the stability and Rashba splitting of the different terminations, we calculated the surface formation energy (SFE) and the Rashba parameter α_R along the high symmetry paths M Γ and MX/MY of the Brillouin zone. The thermodynamic phase diagram results in a narrow region of chemical potentials of Pb and Br in which

MAPbBr₃ is stable. We computed the surface formation energies for points lying in three different regions of chemical potential: Pb and PbBr₂ excess region (point 1), Br and MABr excess region (point 2), and an intermediate point 3 (Fig. S3). Table S4 summarizes the SFE and Rashba parameters for four different terminations of the MAPbBr₃ (100) symmetric slab, two different hydrated terminations, and a stoichiometric asymmetric slab whose formation energy is independent of the Pb and Br chemical potentials. The MABr termination appears to be the most stable of the pristine terminations, consistent with the findings of Meggiolaro *et al.* for MAPbI₃.^{58,59} However, the volatile MA⁺ cations may be removed under thermal annealing or storage, ⁵⁶ and other terminations might become exposed. The Br termination is greatly stabilized under Br and MABr excess conditions.

Our surface energy calculations show that the formation of hydrates is favorable and PbBr₂(H₂O) and MABr(H₂O) are the most stable terminations. The Rashba parameter varies from 0 to 2.02 eV·Å based on the termination and the high symmetry direction. The presence of water indirectly contributes to determining the Rashba splitting by causing distortions in the Pb-Br framework at the surface. The dispersions and splitting along the MX and MY directions are different due to symmetry breaking observed upon ionic relaxation. The Rashba parameter values are generally higher for the CBM due to the large contribution of Pb p states. We find that the highest value of the Rashba parameter in the valence band is 0.96 eV·Å for the MABr termination; the highest value of 2.02 eV·Å is instead found for the conduction band in the case of the PbBr₂ termination. Interestingly, the Rashba parameter is significantly reduced if only the atoms in the first surface layers are allowed to relax, thereby showing the importance of the contribution from the bulk layers (see Tables S2 and S4).

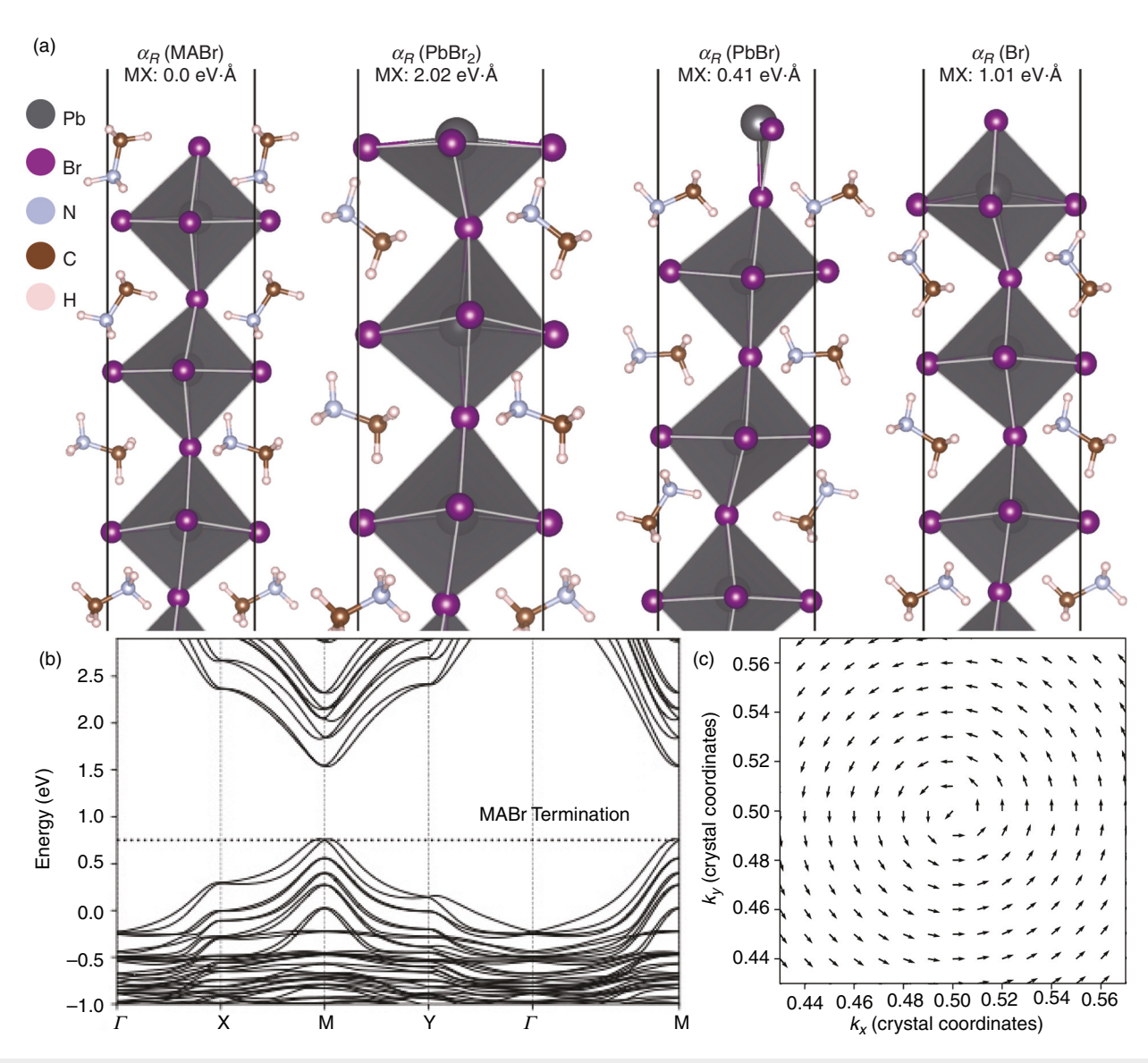


FIG. 6. MAPbBr₃ surface terminations and their Rashba splitting. (a) Different terminations of MAPbBr₃ (100) surface along with a portion of the bulk: MABr, PbBr₂, PbBr, and Br, where the calculated Rashba parameters at the CBM vary significantly. (b) The obtained band structure of one representative, namely, MABr termination. The calculated Rashba parameter, α_R at CBM along with MX and MY direction is $0.00 \text{ eV} \cdot \text{Å}$ and $0.65 \text{ eV} \cdot \text{Å}$, respectively (see Table S4). The Fermi level, shown by the horizontal dotted line, is set to VBM. The high symmetry points are: $\Gamma = (0.0)$, X = (0.5,0), Y = (0.0.5), and M = (0.5,0.5) in crystal coordinates. (c) The calculated spin texture for one of the valence bands at the M point, which is an indication of Rashba splitting. The other valence band has a similar Rashba-like spin texture but with opposite helicity.

Overall, our calculations show that even for the same MAPbBr₃ surface, *there is significant heterogeneity in the Rashba splitting* due to different terminations and non-idealities.

SUMMARY

Our circular photogalvanic effect and spatially resolved photoinduced inverse spin Hall effect measurements provide unambiguous experimental proof for the existence of surface Rashba domains in a cubic MAPbBr₃ single crystal at room temperature, which is due to sample non-idealities. In addition, these measurements unveil the unique spin texture via the Hanle effect, as confirmed by examining the symmetry-breaking features on the crystal surface. Our DFT calculations confirm the formation of different Rashba states, for which strength strongly depends on surface termination, and explain the experimental observation of the Rashba state in nominally HOIPs that possess inversion symmetry. Our work resolves the controversy regarding the Rashba effect in a cubic MAPbBr₃ that possesses inversion symmetry. Our results simultaneously offer a cautionary note in measuring and reporting this important phenomenon in HOIPs as well as in helping to design semiconductor surfaces and various

metal/semiconductor interfaces, which may maximize the Rashba effect even in HOIP materials that nominally do not fulfill conditions for bulk or dynamical Rashba splitting. Our results offer new routes for studying interconversion among photons, charges, and spins in solution-processed compounds. Our findings, and the HOIP materials characterized within, are expected to impact other research areas where HOIPs (e.g., MAPbI₃) are being applied, such as photovoltaic²² and terahertz devices.³⁰

METHODS

Device fabrication

The ITC method was used to grow the MAPbBr₃ single crystal. 0.734 g PbBr₂ and 0.224 g MABr (1:1 molar ratio) were dissolved into 2 ml dimethylformamide to make a 1 M precursor solution. After 24 h of active stirring at room temperature in the nitrogen glovebox (O₂ < 0.1 ppm, $H_2O < 5$ ppm), the clear solution was further filtered with a $0.2 \,\mu m$ polytetrafluoroethylene filter. The glass vial containing the precursor solution was then heated to 80 °C in an oil bath without any disturbance for crystal growth of 8-12 h. When reaching the desired crystal size, the MAPbBr3 single crystal was taken out of the solution in the glovebox and dried with an absorbent paper. Finally, the asgrown single crystal was further dried in a vacuum oven at 60 °C for 12 h before device fabrication. A 5-nm-thick Pt layer was deposited onto the single crystal using electron beam evaporation with a base chamber pressure of 1×10^{-7} Torr and deposition rate of 0.2 Å/s. This very thin layer of Pt (~3 nm) is semi-transparent to optical light illumination.

Device characterization

XRD measurements of the MAPbBr3 single crystal were carried out using a Rigaku SmartLab x-ray diffractometer in a high-resolution setup with a Ge(220) × 2 crystal collimator and a Cu x-ray tube. The XRD data of the powder were acquired using the same diffractometer with a Bragg-Brentano setup. Silver paste was painted onto the two sides of the single crystal with two pieces of copper tape to realize electrical connections. After painting the silver paste, the sample box holding the single crystal was sealed in the N2-filled glovebox with parafilm to reduce the degradation of the material in the atmosphere. The illumination was modulated by an optical chopper at a frequency of 501 Hz. The generated traverse voltage signal in the Pt layer was measured using a lock-in amplifier. The nonvoltaic photocurrent was measured with an SR830 lock-in amplifier. The rotation of the quarter-wave plate was motorized, with a step size equal to 5°. The magnetic field in Hanle effect measurements was generated by an electromagnet (GMW 3470). The spatially resolved photo-ISHE measurements were performed using a 2D X-Y stage with a laser incidence angle of +50°. All the measurements were conducted in ambient conditions at room temperature.

MPM measurements

The MPM measurements were conducted with an erbium-doped femtosecond mode-locked laser operating at 1560 nm, having a pulse duration $\sim\!65$ fs at an average power up to 80 mW with $\sim\!8.5$ MHz repetition rate; hence, the estimated peak power was $\sim\!145$ kW at $\sim\!9$ nJ pulse energy. The laser light was focused ($\sim\!1~\mu\mathrm{m}^2$ spot size) onto the sample, and a half-wave plate and linear polarizer were placed in

front of a beam splitter for power attenuation. A rotatable 870-nm dichroic mirror let the excitation reflection from the sample pass and diverted the resulting THG, SHG, and/or TP-PL onto the photomultiplier tubes (PMTs). A 560-nm dichroic mirror was used to further split the THG to one PMT and the SHG/PL to another PMT. The MPM was collected from the SC surface and bulk separately by moving the focused beam spot in the direction perpendicular to the surface.

DFT calculations

First principle calculations were performed using the plane wave DFT code Quantum Espresso. 60,61 Optimized norm-conserving Vanderbilt (ONCV) pseudopotentials⁶² from the PseudoDojo library⁶ were used for all calculations. For phase diagram and calculation of chemical potentials, the exchange correlation function of Perdew-Burke-Ernzerhof (PBE) generalized gradient approximation⁶⁴ together with DFT-D3 dispersion correction⁶⁵ was used. For calculating Rashba splitting, the results obtained using Heyd-Scuseria-Ernzerhof (HSE) functionals⁶⁶ and PBE with SOC were compared for the non-centrosymmetric bulk structure of MAPbBr₃. The behavior of the bands close to the band edges was very similar (Fig. S6); hence, PBE + SOC was used for obtaining the band structures of surfaces. The Wannier90 package⁶⁷ was used to generate the band structure from HSE calculations. For PBE calculations, we used 14 valence electrons for Pb and 7 valence electrons for Br while for HSE calculations, we used 22 valence electrons for Pb and 17 valence electrons for Br to get the correct bandgap. Energy cutoff values of 75 Ry for the wave function and 300 Ry for charge density were used. Structures were relaxed using a force convergence < 0.001 Ry/ bohr and energy < 0.0001 Ry. A 6 \times 6 \times 6 k-point grid was used for bulk calculations while a $6 \times 6 \times 1$ k-point grid was used for slab calculations. Symmetric slabs of the terminations are used in all simulations and visualized using VESTA.6

SUPPLEMENTARY MATERIAL

See the supplementary material for the XRD, optical microscope images of the MAPbBr₃ single crystals and typical photoluminescence spectrum, angular dependence of the CPGE response in MAPbBr₃ SCs, power dependence of the CPGE and photo-ISHE response, MPM measurements, and DFT calculation details.

AUTHORS' CONTRIBUTIONS

Z.H., S.R.V., T.W., and Z.A. contributed equally to this work. D.S., Z.V.V., and A.A. conceived this study and the experiments. Z.H. was responsible for the CPGE, photo-ISHE, and Hanle effect measurements. S.R.V. was responsible for the MPM measurement and analysis. T.W. provided the single crystals. Z.A. and G.G were responsible for the DFT calculations. Z.H., E.V., X.L., and A.C. fabricated the devices. E.V. and S.Y. measured the Hanle effect. D.S. and E.V. wrote the first draft. D.S., Z.V.V., G.G., and A.A. were responsible for project planning, group managing, and finalizing the manuscript. All authors discussed the results and worked on data analysis and manuscript preparation.

ACKNOWLEDGMENTS

D.S. and A.A. acknowledge support provided by the National Science Foundation (Grant No. ECCS-1936527). The device

fabrication was partially supported by the Department of Energy (Grant No. DE-SC0020992). Z.V.V. and G.G. acknowledge support from the Center for Hybrid Organic Inorganic Semiconductors for Energy (CHOISE), an Energy Frontier Research Center funded by the Office of Basic Energy Sciences, Office of Science, within the U.S. Department of Energy through Contract No. DE-AC36-08G028308. The MPM work was supported in part by the Space Exploration and Optical Solutions Technology Research Initiative Fund (TRIF) at the University of Arizona.

The authors have no conflicts to disclose.

DATA AVAILABILITY

The data that support the findings of this study are available from the corresponding authors upon reasonable request.

REFERENCES

- ¹E. I. Rashba, "Properties of semiconductors with an extremum loop.1. Cyclotron and combinational resonance in a magnetic field perpendicular to the plane of the loop," Sov. Phys. Solid. State 2, 1109 (1960).
- ²R. C. Casella, "Toroidal energy surfaces in crystals with wurtzite symmetry," Phys. Rev. Lett. 5, 371 (1960).
- ³Y. A. Bychkov and E. I. Rashba, "Properties of a 2D electron gas with lifted spectral degeneracy," JETP Lett. **39**, 78 (1984), http://jetpletters.ru/ps/1264/article_19121.shtml.
- ⁴A. Manchon, H. C. Koo, J. Nitta, S. M. Frolov, and R. A. Duine, "New perspectives for Rashba spin–orbit coupling," Nat. Mater. 14, 871 (2015).
- ⁵W. Han, Y. Otani, and S. Maekawa, "Quantum materials for spin and charge conversion," Npj Quantum Mater. 3, 27 (2018).
- ⁶S. D. Stranks and P. Plochocka, "The influence of the Rashba effect," Nat. Mater. 17, 381 (2018).
- ⁷A. Soumyanarayanan, N. Reyren, A. Fert, and C. Panagopoulos, "Emergent phenomena induced by spin-orbit coupling at surfaces and interfaces," Nature 539, 509 (2016).
- ⁸E. Lesne, Y. Fu, S. Oyarzun, J. C. Rojas-Sánchez, D. C. Vaz, H. Naganuma, G. Sicoli, J.-P. Attané, M. Jamet, E. Jacquet, J.-M. George, A. Barthélémy, H. Jaffrès, A. Fert, M. Bibes, and L. Vila, "Highly efficient and tunable spin-to-charge conversion through Rashba coupling at oxide interfaces," Nat. Mater. 15, 1261 (2016).
- ⁹W. Zhang, M. B. Jungfleisch, W. Jiang, J. Sklenar, F. Y. Fradin, J. E. Pearson, J. B. Ketterson, and A. Hoffmann, "Spin pumping and inverse spin hall effects—insights for future spin-orbitronics (Invited)," J. Appl. Phys. 117, 172610 (2015).
- ¹⁰M. M. Lee, J. Teuscher, T. Miyasaka, T. N. Murakami, and H. J. Snaith, "Efficient hybrid solar cells based on meso-superstructured organometal halide perovskites," Science 338, 643 (2012).
- ¹¹H. Zhou, Q. Chen, G. Li, S. Luo, T. Song, H.-S. Duan, Z. Hong, J. You, Y. Liu, and Y. Yang, "Interface engineering of highly efficient perovskite solar cells," Science 345, 542 (2014).
- ¹²W. S. Yang, J. H. Noh, N. J. Jeon, Y. C. Kim, S. Ryu, J. Seo, and S. I. Seok, "High-performance photovoltaic perovskite layers fabricated through intramolecular exchange," Science 348, 1234 (2015).
- ¹³H. Cho, S.-H. Jeong, M.-H. Park, Y.-H. Kim, C. Wolf, C.-L. Lee, J. H. Heo, A. Sadhanala, N. Myoung, S. Yoo, S. H. Im, R. H. Friend, and T.-W. Lee, "Overcoming the electroluminescence efficiency limitations of perovskite light-emitting diodes," Science 350, 1222 (2015).
- ¹⁴R. Younts, H.-S. Duan, B. Gautam, B. Saparov, J. Liu, C. Mongin, F. N. Castellano, D. B. Mitzi, and K. Gundogdu, "Efficient generation of long-lived triplet excitons in 2D hybrid perovskite," Adv. Mater. 29, 1604278 (2017).
- ¹⁵C. Liu, W. Huhn, K.-Z. Du, A. Vazquez-Mayagoitia, D. Dirkes, W. You, Y. Kanai, D. B. Mitzi, and V. Blum, "Tunable semiconductors: Control over carrier states and excitations in layered hybrid organic-inorganic perovskites," Phys. Rev. Lett. 121, 146401 (2018).
- ¹⁶J. Hu, I. W. H. Oswald, S. J. Stuard, M. M. Nahid, N. Zhou, O. F. Williams, Z. Guo, L. Yan, H. Hu, Z. Chen, X. Xiao, Y. Lin, Z. Yang, J. Huang, A. M. Moran,

- H. Ade, J. R. Neilson, and W. You, "Synthetic control over orientational degeneracy of spacer cations enhances solar cell efficiency in two-dimensional perovskites," Nat. Commun. 10, 1276 (2019).
- ¹⁷R. Quintero-Bermudez, A. Gold-Parker, A. H. Proppe, R. Munir, Z. Yang, S. O. Kelley, A. Amassian, M. F. Toney, and E. H. Sargent, "Compositional and orientational control in metal halide perovskites of reduced dimensionality," Nat. Mater. 17, 900 (2018).
- ¹⁸Y. Kutes, L. Ye, Y. Zhou, S. Pang, B. D. Huey, and N. P. Padture, "Direct observation of ferroelectric domains in solution-processed CH₃NH₃PbI₃ perovskite thin films," J. Phys. Chem. Lett. 5, 3335 (2014).
- ¹⁹H. Y. Ye, Y. Y. Tang, P. F. Li, W. Q. Liao, J. X. Gao, X. N. Hua, H. Cai, P. P. Shi, Y. M. You, and R. G. Xiong, "Metal-free three-dimensional perovskite ferroelectrics," Science 361, 151 (2018).
- 20 H. Tsai, W. Nie, J.-C. Blancon, C. C. Stoumpos, R. Asadpour, B. Harutyunyan, A. J. Neukirch, R. Verduzco, J. J. Crochet, S. Tretiak, L. Pedesseau, J. Even, M. A. Alam, G. Gupta, J. Lou, P. M. Ajayan, M. J. Bedzyk, M. G. Kanatzidis, and A. D. Mohite, "High-efficiency two-dimensional Ruddlesden-Popper perovskite solar cells," Nature 536, 312 (2016).
- ²¹M. Kepenekian, R. Robles, C. Katan, D. Sapori, L. Pedesseau, and J. Even, "Rashba and Dresselhaus effects in hybrid organic-inorganic perovskites: From basics to devices," ACS Nano 9, 11557 (2015).
- ²²F. Zheng, L. Z. Tan, S. Liu, and A. M. Rappe, "Rashba spin-orbit coupling enhanced carrier lifetime in CH₂NH₂Pbl₂," Nano Lett. 15, 7794 (2015).
- enhanced carrier lifetime in CH₃NH₃PbI₃," Nano Lett. **15**, 7794 (2015).

 ²³E. Mosconi, T. Etienne, and F. De Angelis, "Rashba band splitting in organohalide lead perovskites: Bulk and surface effects," J. Phys. Chem. Lett. **8**, 2247 (2017)
- ²⁴J. Yin, P. Maity, L. Xu, A. M. El-Zohry, H. Li, O. M. Bakr, J. L. Brédas, and O. F. Mohammed, "Layer-dependent Rashba band splitting in 2D hybrid perovskites," Chem. Mater. 30, 8538 (2018).
- 25 T. Etienne, E. Mosconi, and F. De Angelis, "Dynamical origin of the Rashba effect in organohalide lead perovskites: A key to suppressed carrier recombination in perovskite solar cells?" J. Phys. Chem. Lett. 7, 1638 (2016).
- ²⁶M. Isarov, L. Z. Tan, M. I. Bodnarchuk, M. V. Kovalenko, A. M. Rappe, and E. Lifshitz, "Rashba effect in a single colloidal CsPbBr₃ perovskite nanocrystal detected by magneto-optical measurements," Nano Lett. 17, 5020 (2017).
- 27 Y. Zhai, S. Baniya, C. Zhang, J. Li, P. Haney, C. X. Sheng, E. Ehrenfreund, and Z. V. Vardeny, "Giant Rashba splitting in 2D organic-inorganic halide perovskites measured by transient spectroscopies," Sci. Adv. 3, e1700704 (2017).
- ²⁸D. Niesner, M. Wilhelm, I. Levchuk, A. Osvet, S. Shrestha, M. Batentschuk, C. Brabec, and T. Fauster, "Giant Rashba splitting in CH₃NH₃PbBr₃ organic-inorganic perovskite," Phys. Rev. Lett. 117, 126401 (2016).
- ²⁹D. Niesner, M. Hauck, S. Shrestha, I. Levchuk, G. J. Matt, A. Osvet, M. Batentschuk, C. Brabec, H. B. Weber, and T. Fauster, "Structural fluctuations cause spin-split states in tetragonal (CH3NH3)PbI3; as evidenced by the circular photogalvanic effect," Proc. Natl. Acad. Sci. 115, 9509–9514 (2018).
- ³⁰X. Liu, A. Chanana, U. Huynh, F. Xue, P. Haney, S. Blair, X. Jiang, and Z. V. Vardeny, "Circular photogalvanic spectroscopy of Rashba splitting in 2D hybrid organic-inorganic perovskite multiple quantum wells," Nat. Commun. 11, 323 (2020).
- ³¹B. Wu, H. Yuan, Q. Xu, J. A. Steele, D. Giovanni, P. Puech, J. Fu, Y. F. Ng, N. F. Jamaludin, A. Solanki, S. Mhaisalkar, N. Mathews, M. B. J. Roeffaers, M. Grätzel, J. Hofkens, and T. C. Sum, "Indirect tail states formation by thermal-induced polar fluctuations in halide perovskites," Nat. Commun. 10, 484 (2019).
- ³²K. Frohna, T. Deshpande, J. Harter, W. Peng, B. A. Barker, J. B. Neaton, S. G. Louie, O. M. Bakr, D. Hsieh, and M. Bernardi, "Inversion symmetry and bulk Rashba effect in methylammonium lead iodide perovskite single crystals," Nat. Commun. 9, 1829 (2018).
- ³³C. Wang, B. R. Ecker, H. Wei, J. Huang, J. Q. Meng, and Y. Gao, "Valence band dispersion measurements of perovskite single crystals using angleresolved photoemission spectroscopy," Phys. Chem. Chem. Phys. 19, 5361 (2017).
- ³⁴M. Sajedi, M. Krivenkov, D. Marchenko, A. Varykhalov, J. Sánchez-Barriga, E. D. L. Rienks, and O. Rader, "Absence of a giant Rashba effect in the valence band of lead halide perovskites," Phys. Rev. B. 102, 081116 (2020).
- 35H. Ryu, D. Y. Park, K. M. McCall, H. R. Byun, Y. Lee, T. J. Kim, M. S. Jeong, J. Kim, M. G. Kanatzidis, and J. I. Jang, "Static Rashba effect by surface

- reconstruction and photon recycling in the dynamic indirect gap of APbBr₃ (A = Cs, CH₃NH₃) Single Crystals," J. Am. Chem. Soc. **142**, 21059–21067 (2020).
- ³⁶K. Ando, M. Morikawa, T. Trypiniotis, Y. Fujikawa, C. H. W. Barnes, and E. Saitoh, "Photoinduced inverse spin-Hall effect: Conversion of light-polarization information into electric voltage," Appl. Phys. Lett. 96, 82502 (2010).
- ³⁷K. Ando, M. Morikawa, T. Trypiniotis, Y. Fujikawa, C. H. W. Barnes, and E. Saitoh, "Direct conversion of light-polarization information into electric voltage using photoinduced inverse spin-Hall effect in Pt/GaAs hybrid structure: Spin photodetector," J. Appl. Phys. 107, 113902 (2010).
- ³⁸F. J. Jedema, A. T. Filip, and B. J. van Wees, "Electrical spin injection and accumulation at room temperature in an all-metal mesoscopic spin valve," Nature 410, 345 (2001).
- ³⁹X. Lou, C. Adelmann, S. A. Crooker, E. S. Garlid, J. Zhang, K. S. M. Reddy, S. D. Flexner, C. J. Palmstrøm, and P. A. Crowell, "Electrical detection of spin transport in lateral ferromagnet–semiconductor devices," Nat. Phys. 3, 197 (2007).
- port in lateral ferromagnet–semiconductor devices," Nat. Phys. **3**, 197 (2007).

 40 P. A. Franken, A. E. Hill, C. W. Peters, and G. Weinreich, "Generation of optical harmonics," Phys. Rev. Lett. **7**, 118 (1961).
- ⁴¹S. R. Vardeny, S. Baniya, B. Cromey, K. Kieu, N. Peyghambarian, and Z. V. Vardeny, "Multiphoton microscopy of π -conjugated copolymers and copolymer/fullerene blends for organic photovoltaic applications," ACS Appl. Mater. Interfaces **10**, 31813 (2018).
- ⁴²S. R. Vardeny, S. Baniya, K. Kieu, N. Peyghambarian, and Z. V. Vardeny, "Imaging of π -conjugated polymer/fullerene blends used in organic photovoltaics by nonlinear photoluminescence emission," J. Photonics Energy **9**, 025502 (2019).
- 43 Y. R. Shen, "Surface properties probed by second-harmonic and sum-frequency generation," Nature 337, 519 (1989).
- ⁴⁴E. Saitoh, M. Ueda, H. Miyajima, and G. Tatara, "Conversion of spin current into charge current at room temperature: Inverse spin-Hall effect," Appl. Phys. Lett. 88, 182509 (2006).
- ⁴⁵K. Ando, S. Takahashi, J. Ieda, Y. Kajiwara, H. Nakayama, T. Yoshino, K. Harii, Y. Fujikawa, M. Matsuo, S. Maekawa, and E. Saitoh, "Inverse spin-Hall effect induced by spin pumping in metallic system," J. Appl. Phys. 109, 103913 (2011).
- ⁴⁶ X. W. He, B. Shen, Y. H. Chen, Q. Zhang, K. Han, C. M. Yin, N. Tang, F. J. Xu, C. G. Tang, Z. J. Yang, Z. X. Qin, G. Y. Zhang, and Z. G. Wang, "Anomalous photogalvanic effect of circularly polarized light incident on the two-dimensional electron gas in AlxGa_{1-x}N/GaN heterostructures at room temperature," Phys. Rev. Lett. 101, 147402 (2008).
- ⁴⁷D. Sun, C. Zhang, M. Kavand, J. Wang, H. Malissa, H. Liu, H. Popli, J. Singh, S. R. Vardeny, W. Zhang, C. Boehme, and Z. V. Vardeny, "Surface-enhanced spin current to charge current conversion efficiency in CH₃NH₃PbBr₃-based devices," J. Chem. Phys. 151, 174709 (2019).
- ⁴⁸J. Wang, C. Zhang, H. Liu, R. McLaughlin, Y. Zhai, S. R. Vardeny, X. Liu, S. McGill, D. Semenov, H. Guo, R. Tsuchikawa, V. V. Deshpande, D. Sun, and Z. V. Vardeny, "Spin-optoelectronic devices based on hybrid organic-inorganic trihalide perovskites," Nat. Commun. 10, 129 (2019).
- ⁴⁹S. Yang, E. Vetter, T. Wang, A. Amassian, and D. Sun, "Observation of long spin lifetime in MAPbBr₃ single crystals at room temperature," J. Phys. Mater. 3, 15012 (2020).
- ⁵⁰W. Yang, Q. Shi, T. Miao, Q. Li, P. Cai, H. Liu, H. Lin, Y. Bai, Y. Zhu, Y. Yu, L. Deng, W. Wang, L. Yin, D. Sun, X.-G. Zhang, and J. Shen, "Achieving large and nonvolatile tunable magnetoresistance in organic spin valves using electronic phase separated manganites," Nat. Commun. 10, 3877 (2019).
- ⁵¹C. Zhang, D. Sun, C.-X. Sheng, Y. X. Zhai, K. Mielczarek, A. Zakhidov, and Z. V. Vardeny, "Magnetic field effects in hybrid perovskite devices," Nat. Phys. 11, 427 (2015).
- ⁵²O. Yaffe, Y. Guo, L. Z. Tan, D. A. Egger, T. Hull, C. C. Stoumpos, F. Zheng, T. F. Heinz, L. Kronik, M. G. Kanatzidis, J. S. Owen, A. M. Rappe, M. A. Pimenta, and L. E. Brus, "Local polar fluctuations in lead halide perovskite crystals," Phys. Rev. Lett. 118, 136001 (2017).
- ⁵³L. Leppert, S. E. Reyes-Lillo, and J. B. Neaton, "Electric field- and strain-induced Rashba effect in hybrid halide perovskites," J. Phys. Chem. Lett. 7, 3683 (2016).

- ⁵⁴P. C. Sercel, Z. V. Vardeny, and A. L. Efros, "Circular dichroism in non-chiral metal halide perovskites," Nanoscale 12, 18067 (2020).
- 55S. Y. Leblebici, L. Leppert, Y. Li, S. E. Reyes-Lillo, S. Wickenburg, E. Wong, J. Lee, M. Melli, D. Ziegler, D. K. Angell, D. F. Ogletree, P. D. Ashby, F. M. Toma, J. B. Neaton, I. D. Sharp, and A. Weber-Bargioni, "Facet-dependent photovoltaic efficiency variations in single grains of hybrid halide perovskite," Nat. Energy 1, 16093 (2016).
- 56J. Huang, Y. Yuan, Y. Shao, and Y. Yan, "Understanding the physical properties of hybrid perovskites for photovoltaic applications," Nat. Rev. Mater. 2, 17042 (2017).
- 57B. Murali, S. Dey, A. L. Abdelhady, W. Peng, E. Alarousu, A. R. Kirmani, N. Cho, S. P. Sarmah, M. R. Parida, M. I. Saidaminov, A. A. Zhumekenov, J. Sun, M. S. Alias, E. Yengel, B. S. Ooi, A. Amassian, O. M. Bakr, and O. F. Mohammed, "Surface restructuring of hybrid perovskite crystals," ACS Energy Lett. 1, 1119 (2016).
- ⁵⁸D. Meggiolaro, E. Mosconi, A. H. Proppe, R. Quintero-Bermudez, S. O. Kelley, E. H. Sargent, and F. De Angelis, "Energy level tuning at the MAPbI₃ perovskite/contact interface using chemical treatment," ACS Energy Lett. 4, 2181 (2019).
- ⁵⁹C. W. Myung, S. Javaid, K. S. Kim, and G. Lee, "Rashba–Dresselhaus effect in inorganic/organic lead iodide perovskite interfaces," ACS Energy Lett. 3, 1294 (2018).
- 60 P. Giannozzi, S. Baroni, N. Bonini, M. Calandra, R. Car, C. Cavazzoni, D. Ceresoli, G. L. Chiarotti, M. Cococcioni, I. Dabo, A. Dal Corso, S. de Gironcoli, S. Fabris, G. Fratesi, R. Gebauer, U. Gerstmann, C. Gougoussis, A. Kokalj, M. Lazzeri, L. Martin-Samos, N. Marzari, F. Mauri, R. Mazzarello, S. Paolini, A. Pasquarello, L. Paulatto, C. Sbraccia, S. Scandolo, G. Sclauzero, A. P. Seitsonen, A. Smogunov, P. Umari, and R. M. Wentzcovitch, "QUANTUM ESPRESSO: A modular and open-source software project for quantum simulations of materials," J. Phys. Condens. Matter 21, 395502 (2009).
- ⁶¹P. Giannozzi, O. Andreussi, T. Brumme, O. Bunau, M. Buongiorno Nardelli, M. Calandra, R. Car, C. Cavazzoni, D. Ceresoli, M. Cococcioni, N. Colonna, I. Carnimeo, A. Dal Corso, S. de Gironcoli, P. Delugas, R. A. DiStasio, A. Ferretti, A. Floris, G. Fratesi, G. Fugallo, R. Gebauer, U. Gerstmann, F. Giustino, T. Gorni, J. Jia, M. Kawamura, H.-Y. Ko, A. Kokalj, E. Küçükbenli, M. Lazzeri, M. Marsili, N. Marzari, F. Mauri, N. L. Nguyen, H.-V. Nguyen, A. Otero-de-la-Roza, L. Paulatto, S. Poncé, D. Rocca, R. Sabatini, B. Santra, M. Schlipf, A. P. Seitsonen, A. Smogunov, I. Timrov, T. Thonhauser, P. Umari, N. Vast, X. Wu, and S. Baroni, "Advanced capabilities for materials modelling with Quantum ESPRESSO," J. Phys. Condens. Matter 29, 465901 (2017).
- ⁶²D. R. Hamann, "Optimized norm-conserving Vanderbilt pseudopotentials," Phys. Rev. B 88, 085117 (2013).
- ⁶³M. J. van Setten, M. Giantomassi, E. Bousquet, M. J. Verstraete, D. R. Hamann, X. Gonze, and G.-M. Rignanese, "The PseudoDojo: Training and grading a 85 element optimized norm-conserving pseudopotential table," Comput. Phys. Commun. 226, 39 (2018).
- 64 J. P. Perdew, K. Burke, and M. Ernzerhof, "Generalized gradient approximation made simple," Phys. Rev. Lett. 77, 3865 (1996).
- 65S. Grimme, J. Antony, S. Ehrlich, and H. Krieg, "A consistent and accurate ab initio parametrization of density functional dispersion correction (DFT-D) for the 94 elements H-Pu," J. Chem. Phys. 132, 154104 (2010).
- ⁶⁶J. Heyd, G. E. Scuseria, and M. Ernzerhof, "Hybrid functionals based on a screened coulomb potential," J. Chem. Phys. 118, 8207 (2003).
- ⁶⁷G. Pizzi, V. Vitale, R. Arita, S. Blügel, F. Freimuth, G. Géranton, M. Gibertini, D. Gresch, C. Johnson, T. Koretsune, J. Ibañez-Azpiroz, H. Lee, J.-M. Lihm, D. Marchand, A. Marrazzo, Y. Mokrousov, J. I. Mustafa, Y. Nohara, Y. Nomura, L. Paulatto, S. Poncé, T. Ponweiser, J. Qiao, F. Thöle, S. S. Tsirkin, M. Wierzbowska, N. Marzari, D. Vanderbilt, I. Souza, A. A. Mostofi, and J. R. Yates, "Wannier90 as a community code: New features and applications," J. Phys. Condens. Matter 32, 165902 (2020).
- ⁶⁸K. Momma and F. Izumi, "VESTA 3 for Three-dimensional visualization of crystal, volumetric and morphology data," J. Appl. Crystallogr. 44, 1272 (2011).